View Article Online
View Journal

Journal of Materials Chemistry C

Materials for optical, magnetic and electronic devices

Accepted Manuscript

This article can be cited before page numbers have been issued, to do this please use: Z. Zhu, W. Li, W. Deng, W. He, C. Yan, X. Peng, X. Zeng, Y. Gao, X. Fu, N. Lin, B. Gao and W. Yang, *J. Mater. Chem. C*, 2022, DOI: 10.1039/D2TC00235C.

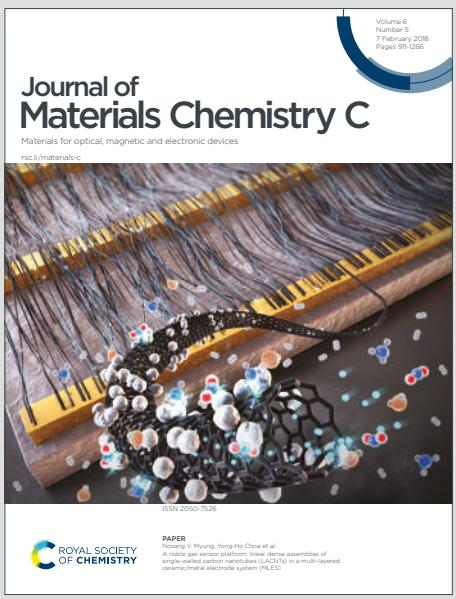

ROYAL SOCIETY OF CHEMISTRY

rsc.li/materials-c

View Article Online
DOI: 10.1039/D2TC00235C

Controllably metastable growth of perovskite single crystals for highly sensitive X-ray detection

Zhihao Zhu, Wen Li, Wen Deng, Weidong He, Cheng Yan, Xiaodong Peng, Xiankan Zeng, Yue Gao, Xuehai Fu, Na Lin, Bo Gao* and Weiqing Yang**

Z. Zhu, Asso. Prof. N. Lin, Asso. Prof. B. Gao

Institute of Materials, China Academy of Engineering Physics, Jiangyou 621907, China

E-mail: nalin_2016@163.com; 11409745@qq.com

Z. Zhu, Dr. W. Li, C. Yan, X. Peng, X. Zeng, Y. Gao, X. Fu, Prof. W. Yang

Key Laboratory of Advanced Technologies of Materials (Ministry of Education), School of Materials Science and Engineering, Southwest Jiaotong University, Chengdu 610031, China

E-mail: wqyang@swjtu.edu.cn

W. Deng

Hunan Key Laboratory of Super Microstructure and Ultrafast Process, School of Physics and Electronics, Central South University, Changsha, Hunan 410083, China.

Prof. W. He

National Key Laboratory of Science and Technology on Advanced Composites in Special Environments, and Center for Composite Materials and Structures, Harbin Institute of Technology, Harbin 150080, China.

key words: perovskite, $MAPbBr_3$, single crystal, crystallization, X-ray detector.

Abstract

Single crystalline perovskites with long carrier lifetime, large carrier mobility and high atomic number emerge as highly sensitive X-ray detection materials. To precisely control its growth for high-quality perovskites single crystals (SCs) is still a big challenge to date. Herein, a simple, convenient and highly-reproducible method, low-

temperature controllable metastable crystallization (LCMC), is shown to prepare high-quality $CH_3NH_3PbBr_3$ ($MAPbBr_3$) SCs at low temperature of 45 °C. A surprisingly reduced full width at half-maximum of the (001) and (002) planes and hence a higher crystalline quality for the LCMC-$MAPbBr_3$ SCs as compared to the inverse temperature crystallization (ITC) SCs. Moreover, the LCMC-$MAPbBr_3$ SCs possess longer carrier lifetime increased by nearly 248% to 1126 ns, larger carrier mobility increased by 146% to 87.8 $cm^2\ V^{-1}\ s^{-1}$, and significantly lower trap density of 2.1×10^9 cm^{-3} (reduced by around 89%) compared with the ITC samples. Based on the high-quality SCs, the as-developed X-ray detector demonstrate a high sensitivity of 2975.7 $\mu C\ Gy_{air}^{-1}\ cm^{-2}$ and a lowest detectable dose rate of 0.48 $\mu Gy_{air}\ s^{-1}$. Evidently, this work may pave a way for controlling the crystallization process of perovskites, which is essential for enhancing the further applications of perovskite SCs.

Introduction

Sensitive semiconductor X-ray detector is of great significance for broad applications such as medical imaging, security screening, shipping container inspection, defect inspection and quality control.[1–3] Different from the indirect scintillator detection method of converting X-ray into visible light, the semiconductor X-ray detector can directly convert X-ray into electron-hole pairs and naturally possess higher spatial resolution and simpler system configuration.[4] In general, high sensitivity, a key parameter in X-ray detectors, which facilitates the reduction of X-ray dose in medical treatment and environmental security applications, is closely related to the carrier mobility, carrier lifetime and atomic number of the semiconductor material.[5–7]

Among the semiconductor materials, the organic-inorganic perovskites (ABX_3, A = $CH_3NH_3^+$, $CH(NH_2)_2^+$, B = Pb^{2+}, Sn^{2+}, X = Cl^-, Br^-, I^-) are considered as promising candidates for X-ray detection.[8, 9] They inherently combine excellent radiation detection properties such as high atomic number (elements Pb, I and Br), high carrier mobility, long carrier lifetime, and low defect density.[10–12] Compared to polycrystalline films, perovskite single crystals (SCs) show even better intrinsic properties.[13–15] Hybrid

perovskite SCs have been successfully prepared with various solution-based methods, such as inverse temperature crystallization (ITC),[16, 17] solution temperature lowering (STL) method,[18, 19] anti-solvent vapor-assisted crystallization (AVC),[20] and slow evaporation (SE) method.[21] Unfortunately, their crystallization qualities are still not adequate for extremely harsh applications, such as highly sensitive X-ray detection.[22, 23] For example, the conventional ITC method uses a fixed growth temperature, the growth rate varies greatly with time due to the decrease of solute concentration, and the single crystal is grown at a high temperature above 80 °C. These may lead to undesired defects in the crystal structure. In order to obtain high-quality perovskite SCs, it is necessary to carefully regulate the growth conditions within the metastable zone, the most ideal region for SCs growth, where only pre-existing crystal (pre-selected seed crystal) grow and no new crystals are formed.[24] Moreover, perovskite SCs grown at low temperatures have been proved to result in significantly lower trap density and higher optoelectronic properties compared with those at high temperatures.[25–28] However, there is still no effective method to stably control the synthesize of high-quality perovskite SCs at low temperature.

Here, we developed a formic-acid-assisted metastable crystallization (LCMC) method for growing high-quality $CH_3NH_3PbBr_3$ ($MAPbBr_3$) SCs at low temperature. This LCMC method enables the low temperature preparation of $MAPbBr_3$ SCs by adding formic acid (FA) into the precursor solution as it reduces the solubility of $MAPbBr_3$ in *N*,*N*-dimethylformamide (DMF), leading to the supersaturated solution at lower temperature. Furthermore, maintaining a slightly supersaturated solution by manipulating the temperature ramp-up rate, i.e.; keeping the entire growth process strictly within the metastable zone, ensured a consistently low crystal growth rate and suppressed additional nucleation. Finally, high quality $MAPbBr_3$ SCs with low trap density (2.1×10^9 cm^{-3}) were obtained at low temperature of 45 °C. The crystallization kinetics via the LCMC strategy were investigated in detail. Moreover, the LCMC-$MAPbBr_3$ SCs exhibit a longer lifetime of 1126 ns and a larger carrier mobility of 87.8 cm^2 V^{-1} s^{-1} compared to those prepared at high temperature of 80 °C (324 ns and 35.7 cm^2 V^{-1} s^{-1}). In addition, the as-developed X-ray detectors exhibit excellent sensitivity

(2975.7 μC Gy_{air}^{-1} cm^{-2}) and extremely low X-ray dose rates (the lowest detectable X-ray dose rate is 0.48 μGy_{air} s^{-1}). This work provides a strategy for preparing high-quality perovskite SCs, which further promotes the development of perovskite photovoltaic devices.

Experimental section

Materials.

Lead bromide ($PbBr_2$, 99.99%), Methylammonium bromide (MABr, 99.9%), *N*, *N*-dimethylformamide (DMF, 99%), and formic acid (FA, 99%). All salts and solvents were used without any further purification.

Preparation of LCMC $MAPbBr_3$ single crystals.

1.835 g $PbBr_2$ and 0.56 g MABr (1:1 molar ratio) were dissolved in 5 mL DMF (equivalent to 1 M $MAPbBr_3$ in DMF) at room temperature under active mixing for 24 h, followed by filtration through a 0.22 μm pore size filter. 400 μl of formic acid was added, stirred for 15 minutes and filtered again. The washed silicon wafer was immersed into the solution and the pre-selected seed crystal was then carefully placed on the wafer. The initiate temperature of the solution was set at 25 °C and then ramped up to 45 °C after 12 h at a rate of 2 °C day^{-1}. Finally, A high-quality $MAPbBr_3$ SC was obtained.

Solubility test.

The solubility test was carried out according to a previously reported method.[33] First, $MAPbBr_3$ single crystals were cleaned and dried with toluene and then milled into powder. 4 mL of DMF was kept at the test temperature. $MAPbBr_3$ powder was added with stirring, 0.06 g at a time, until the solution reached supersaturation. When the powder was not completely dissolved even after 30 minutes of addition, the solution was assumed to be supersaturated and the total mass of the added powder was recorded. Repeat the above procedure at different test temperatures to obtain the solubility data at all required temperatures. The solubility test after the addition of formic acid requires only a mixture of DMF and formic acid instead of pure DMF. Finally, the solubility curves were obtained by fitting the data.

View Article Online
DOI: 10.1039/D2TC00235C

Fabrication of devices for SCLC measurements.

The devices were fabricated by depositing the Au electrodes (approximately 100 nm thickness) with the architecture of Au/$MAPbBr_3$ SC/Au.

Fabrication of the $MAPbBr_3$ SC X-ray detector.

Detectors with vertical structure of Au/$MAPbBr_3$ SC/Ag were fabricated by depositing 150 nm thick Au and Ag electrodes on opposite sides of the SC, respectively, by vacuum evaporation method.

High-resolution XRD analysis.

The high-resolution XRD rocking curves of the $MAPbBr_3$ SCs were carried out by the Bruker D8 DISCOVER (Germany) X-ray diffract meter with Cu $K_{\alpha 1}$ radiation (λ = 1.54056 nm).

Absorbance measurements.

The UV-vis absorption spectrum was recorded by using a Perkin-Elmer Lambda 1050 UV-vis spectrophotometer operating in the 190–900 nm region at room temperature.

Steady-state and time resolved photoluminescence measurements.

The steady-state and time resolved photoluminescence measurements of $MAPbBr_3$ SCs were examined using a FLS 980 (Edinburgh Instruments) spectrometer.

SCLC measurements.

The single carrier devices were fabricated and used to measure the trap-state density by using the SCLC method for the $MAPbBr_3$ SCs. The dark *I-V* curves were measured using the Keithley 4200 semiconductor characterization system at room temperature and was used to calculate the trap-state density. The thicknesses of the $MAPbBr_3$ SCs were measured by a digital vernier caliper.

X-ray response measurements.

The current-voltage and current-time characteristics of the detectors were recorded by a Keithley 6430 source meter under X-ray radiation. The X-ray source is a commercially available X-ray tube (0150, Harmonious) with a tube voltage range of 40–120 kV and a maximum output power of 5 kW. In addition, several pieces of 2 mm thick Al foil were inserted between the source and the detector as attenuators.

View Article Online
DOI: 10.1039/D2TC00235C

Results and discussion

Fig. 1a schematically shows the LCMC preparation of $MAPbBr_3$ SCs at low temperature. In brief, $PbBr_2$ and MABr (1:1 molar ratio) were dissolved in DMF at room temperature under active mixing for 24 h for the 1 M $MAPbBr_3$ precursor solution (Fig. 1a-i). Then, 8 vol% formic acid was added into the precursor solution (Fig. 1a-ii). After filtration, a pre-selected seed crystal (obtained by supersaturating the precursor solution firstly) was placed on the silicon wafer and completely immersed into the solution (Fig. 1a-iii), which was placed at 25 °C for 12 h and then slowly heated to 45 °C with a temperature ramping rate of 2 °C day^{-1} (Fig. 1a-iv). After approximately 10 days, a large $MAPbBr_3$ SC (7 mm × 7 mm × 3 mm) was harvested (Fig. 1a-v). The growth device and single crystal photographs are shown in Fig. S1 (ESI).

In general, the crystallization process mainly consists of two steps, namely nucleation and crystal growth. The driving force of the crystallization process is the supersaturation of the metastable precursor solution, which is mainly determined by temperature and concentration.[25] The whole growth model of the solution-based approach can be demonstrated using a dissolution-nucleation diagram (Fig. 1b), which is mainly divided into the unsaturated, metastable and unstable zones by the solubility curve and nucleation curve (solubility + ΔS). In the unsaturated zone, crystals cannot be formed according to the definition of unsaturated solution. Even if seed crystals are put in, they will not grow; instead, they will gradually dissolve into the solution. While in the metastable zone, spontaneous crystallization does not occur but existing crystals can grow up due to the low level of supersaturation. In contrast, there is a large supersaturation in the unstable zone, where spontaneous nucleation as well as crystal growth exists. These can be explained by a classical nucleation theory, according to which the nucleation rate j_0 can be expressed by the equation[29, 30]

$$j_0 = A \cdot \exp\left(-\frac{\Delta G_{\mathrm{N}}}{k_{\mathrm{B}}T}\right) \tag{1}$$

where A is the pre-exponential factor, ΔG_{N} is the nucleation energy barrier or Gibbs free energy change for the nucleus formation, k_{B} is the Boltzmann constant, T is the

temperature. When the solution is supersaturated enough to overcome the nucleation barrier and the simultaneous formation of nuclei with radii greater than the critical nucleation radius (r_0), these nuclei will spontaneously grow into larger crystals (Fig. S2, ESI).[31, 32] Although the precursor solution in the metastable zone is supersaturated, the solution system possesses insufficient energy to overcome the nucleation barrier and then the nucleation rate is almost zero. Since there is no additional nucleation, the selected crystallite as seed crystal can grow individually in this region without being affected by newly formed crystals, making this zone the most suitable region for the preparation of perovskite SCs. While in the unstable zone, the solution is supersaturated enough for spontaneous nucleation. Crystallites are continuously formed until the concentration of the solution is reduced to the metastable region. Crystals formed by subsequent nucleation will grow together with the already existing crystals, reducing the size of the resulting crystals and possibly forming twinning defects. Therefore, metastable zone is undoubtedly the most desirable region for preparing high-quality perovskite SCs.

View Article Online
DOI: 10.1039/D2TC00235C

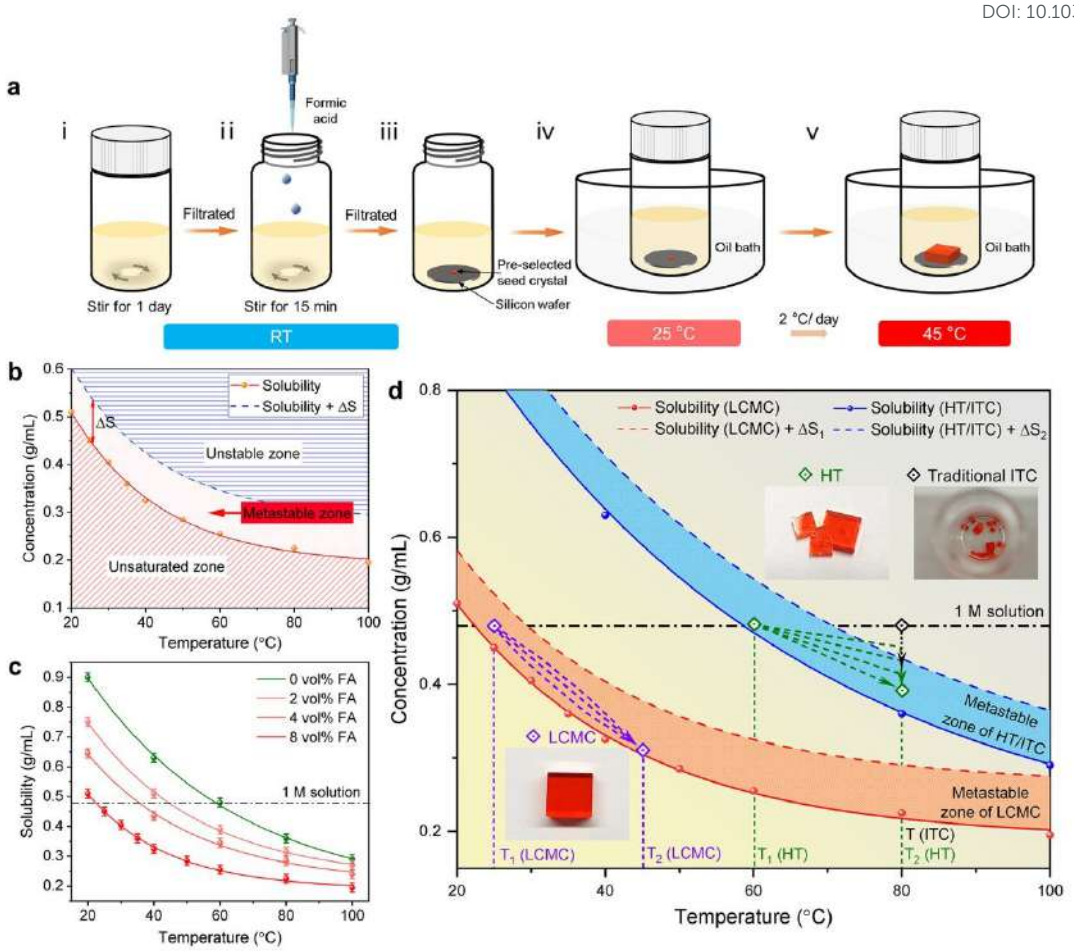

Fig. 1. Crystallization of the $MAPbBr_3$ SCs. (a) Schematic illustration of the LCMC process. (b) Temperature-dependent solubility curve for different regions in the supersaturation model. (c) Temperature-dependent solubility of $MAPbBr_3$ in DMF with different addition of formic acid from 0 to 8 vol%. (d) Dissolution–nucleation diagram. Purple arrow with short dashed line: LCMC method. Green arrow with short dashed line: HT method. Black arrow with dot line: traditional ITC method.

To achieve low temperature preparation of $MAPbBr_3$ SCs, FA is added into the precursor solution. The addition of FA alters the acid-base equilibrium, causing the colloid to dissolve and release the solute contained therein, thus increasing the solute concentration and also reducing the strength of the solvent, leading to supersaturation at lower temperature and subsequent crystallization.[25] To precisely regulate the growth process of $MAPbBr_3$ SCs, the solubility of $MAPbBr_3$ in DMF solvents with different volume percentages of FA was investigated in the range of 20 to 100 °C using a method

reported in the literature (Fig. 1c).[33] The phenomenon of inverse solubility was observed in the solubility curves. Meanwhile, the solubility curve and slope decreased significantly as the volume percentage of formic acid increased. Based on the solubility data in the temperature range of 20–100 °C, the solubility curves were numerically simulated using power series as shown in Fig. S3 (ESI). It is worth noting that the precursor solution (1 M) with the addition of 8% volume percentage (8 vol%) FA is close to supersaturation at room temperature, indicating $MAPbBr_3$ SCs could be prepared at a relatively low temperature.

Due to the phenomenon of retrograde solubility of $MAPbBr_3$ in DMF, the fast and convenient crystallization method, inverse temperature crystallization (ITC), has been widely used, demonstrating an order of magnitude faster than other classical crystallization methods and ensuring comparable crystal quality.[13, 16] The LCMC method was preceded by attempts to prepare single crystals using the conventional ITC method as well as the optimized ITC method with temperature gradient crystallization.[34, 35] The concentration-temperature diagram of the above crystallization methods is shown in Fig. 1d. For the conventional ITC method, new nuclei were continuously generated as the starting growth conditions (1 M, 80 °C) were in the unstable zone. The crystallization process is difficult to control, and even if the growth temperature is lowered to 73 °C by optimization, 1–3 crystals are randomly produced. In addition, the crystallization yield is low due to the fixed growth temperature. Moreover, as the solute is consumed during crystal growth, the difference between solute concentration and solubility decreases quickly, thus the growth rate varies greatly with time. For the optimized ITC method with temperature gradient crystallization, $MAPbBr_3$ SCs were prepared in a similar way to the literatures, which is noted as HT method.[16, 34] Although the HT method avoids large growth rate variations and increases the crystallization yield, due to the rapid ramp rate, extraneous crystals are still formed in some samples as the growth entered into the unstable zone, leading to the uncontrolled growth. These newly formed crystals may stack with the seed crystal, thus forming twinning defects. Notably, for the growth of LCMC-$MAPbBr_3$ SCs, no additional crystallization was observed during the growth of all samples and the

obtained crystals did not have any observable cracks. This is attributed to the system was strictly controlled in the metastable zone to suppress the extraneous nucleation and to ensure continuous growth of the seed crystal by using the slow temperature ramping rate.

To further investigate the magnitude and variation of the growth rate during the crystallization of $MAPbBr_3$ SCs, the crystal growth rate was calculated by the supersaturation model[36]

$$\frac{\mathrm{d}m}{\mathrm{d}t} = -\frac{1}{2}V \cdot \frac{\mathrm{d}C(T)}{\mathrm{d}t} = -\frac{1}{2}V \cdot \frac{\mathrm{d}C(T)}{\mathrm{d}T}\frac{\mathrm{d}T}{\mathrm{d}t} \tag{2}$$

where m is the mass of the crystal, C is the solution concentration, and V is the solution volume. For LCMC method, the solution volume varies very little during the entire process. Hence, it can be considered as a constant. Also, $\mathrm{d}T/\mathrm{d}t$ is precisely controlled as a constant of 2 °C day^{-1}, and $\mathrm{d}C(T)/\mathrm{d}T$ is obtained by using the fitted solubility curve equation (Fig. S3a, ESI). The growth rate corresponding to different temperatures during the preparation can be calculated (Fig. S4a, ESI). Subsequently, the growth rate can be obtained as a function of time according to the temperature ramping rate, as shown in Fig. S4b (ESI). For comparison, the growth rate of the HT method is also shown in Fig. S4 (ESI), with the LCMC method exhibiting significantly lower growth rate and smaller growth rate variation. Generally, for crystal growth, the slower the growth rate, the higher the quality.[25] Moreover, the theoretical crystallization yields for the LCMC and HT methods were calculated based on the solubility curves, as shown in Fig. S5 (ESI). Obviously, the HT method is unable to prepare $MAPbBr_3$ SCs at low temperature lower than 60 °C, and the LCMC method exhibits significantly higher crystallization yield at the same temperature. The crystallization yield of the LCMC method is 36.4% at a growth termination temperature of 45 °C, while the HT method can only reach 24.4% at a higher termination temperature of 80 °C.

View Article Online
DOI: 10.1039/D2TC00235C

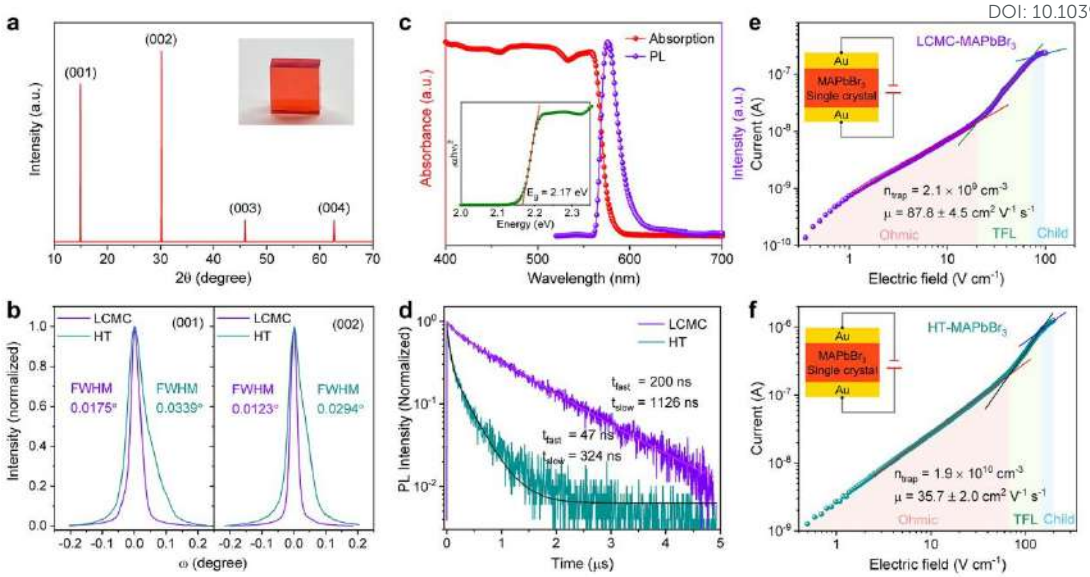

Fig. 2. Characterization of the $MAPbBr_3$ SCs. (a) XRD 2θ scans of the $MAPbBr_3$ SC grown using the LCMC method. (b) High-resolution XRD rocking curve of the (001) and (002) diffraction peaks of the $MAPbBr_3$ SCs grown using the LCMC and HT methods. (c) Absorption and PL spectra of the LCMC-$MAPbBr_3$ SC. (d) Time-resolved PL of the $MAPbBr_3$ SCs. Characteristic *I-E* curves of the (e) LCMC-$MAPbBr_3$ and (f) HT-$MAPbBr_3$ SCs.

To further investigate the quality of the $MAPbBr_3$ SCs prepared by the LCMC and HT methods, the X-ray diffraction (XRD) measurement were conducted. In Fig. 2a, the X-ray 2θ scan on the maximal facet of the LCMC-$MAPbBr_3$ SCs shows sharp peaks at 14.96°, 30.16°, 45.92°, and 62.68°, respectively, corresponding to the (001), (002), (003), and (004) planes of the cubic phase of $MAPbBr_3$ crystal structure.[37, 38] Moreover, the only four diffraction peaks indicating the achievement of well-structured single-crystalline $MAPbBr_3$. Furthermore, the (001) and (002) peaks were carefully analyzed using high-resolution X-ray rocking curve (Fig. 2b). The full width at half maximum (FWHM) of (001) and (002) peaks for the LCMC-$MAPbBr_3$ SCs are as narrow as 0.0175° and 0.0123°, respectively. These values are 48% and 58% lower than that of the HT-$MAPbBr_3$ SCs, i.e.; 0.0339° and 0.0294° for the (001) and (002) peaks, respectively. It is indicated that the LCMC-$MAPbBr_3$ SCs possess higher crystal quality and superiority of the LCMC method. The surface morphology of the as-prepared

MAPbBr$_3$ SCs were investigated by atomic force microscopy (AFM). The LCMC-MAPbBr$_3$ SC have a flat top surface and a relatively uniform height distribution, as confirmed by AFM height images (Fig. S6, ESI). The root-mean-square roughness (R_q) values were 4.3 and 7.5 nm for the LCMC-MAPbBr$_3$ SC and HT-MAPbBr$_3$ SC, respectively.

Fig. 2c displays the steady-state absorption spectrum and the steady-state photoluminescence (PL) spectrum of the MAPbBr$_3$ SCs. The steady-state absorption spectrum exhibits a sharp absorption edge at 590 nm, indicating a bandgap of 2.17 eV, which is in agreement with the literature.[17] The PL peak is located at 578 nm with a narrow FWHM of 21 nm. The PL peak is smaller than the onset of absorption, indicating the light of PL due to the excitation can be self-extinguished.[35] Furthermore, the PL lifetimes of the LCMC-MAPbBr$_3$ and HT-MAPbBr$_3$ SCs were investigated using time-resolved photoluminesce (TRPL) spectroscopy. The two exponential carrier lifetimes were obtained by fitting the TRPL results to a two exponential decay model. The fast and slow decay lifetimes will correspond to the recombination of surface carriers and bulk carriers, respectively.[39, 40] This is in good agreement with the recently-reported ones for the same kind of SCs.[16, 41] As shown in Fig. 2d, the LCMC-MAPbBr$_3$ SC exhibits a significantly longer fast decay lifetime of 200 ns and a slow decay lifetime of 1126 ns in contrast with that of HT-MAPbBr$_3$ SC (47 ns for fast decay lifetime and 324 ns for slow decay lifetime), indicating that the LCMC-MAPbBr$_3$ SCs has fewer traps. Additionally, the LCMC-MAPbBr$_3$ SCs demonstrate significantly improved average carrier lifetime (1097 ± 230 ns) in contrast to that of the HT-MAPbBr$_3$ SCs (306 ± 42 ns), as shown in Fig. S7 (ESI).

The trap density (n_{trap}) of MAPbBr$_3$ SCs was investigated using the space charge limited current (SCLC) method.[42, 43] Devices with Au/MAPbBr$_3$ SC/Au sandwich architecture were fabricated for testing. Fig. 2e and f demonstrate the dark *I-E* characteristics of the LCMC-MAPbBr$_3$ and HT-MAPbBr$_3$ SCs, respectively. Each *I-E* traces is divided into three regions: the lower bias is the ohmic region, the higher bias is the child region, and the intermediate bias is the trap-filled region, separated from the ohmic region at the trap-filled limit voltage, where the current dramatically increases

with bias increasing. Subsequently, the trap density (n_{trap}) can be extracted by using the formula[42, 43]

$$n_{trap} = \frac{2\varepsilon_0 \varepsilon_r V_{TFL}}{qL^2} \quad (3)$$

where ε_0 represents the vacuum permittivity, ε_r is the relative dielectric constant (ε_r = 25.5)[44], V_{TFL} is the trap-filled limit voltage, q is the elementary charge, and L is the thickness of the $MAPbBr_3$ SCs. According to the SCLC model, the n_{trap} is determined to be 1.9×10^{10} cm^{-3} for HT-$MAPbBr_3$ SC, while it is only 2.1×10^9 cm^{-3} for LCMC-$MAPbBr_3$ one. Significantly, the n_{trap} of the LCMC-$MAPbBr_3$ SC is seven orders of magnitude lower than that of its polycrystalline counterparts (~10^{16} cm^{-3}).[20, 45]

Furthermore, the carrier mobility of the $MAPbBr_3$ SCs was calculated by fitting the Child region according to the Mott-Gurney law[46, 47]

$$\mu = \frac{8J_d L^3}{9\varepsilon_0 \varepsilon_r V^2} \quad (4)$$

where J_d is the dark current density, V is the applied voltage. The carrier mobility of LCMC-$MAPbBr_3$ SC is extracted as 87.8 ± 4.5 cm^2 V^{-1} s^{-1}, while that of HT-$MAPbBr_3$ SC was only 35.7 ± 2.0 cm^2 V^{-1} s^{-1}. Such ultralow trap density and excellent carrier mobility indicate superior crystal quality for the LCMC-$MAPbBr_3$ SC. Moreover, the conductivity and hole concentration identified from the linear ohmic region are $\sigma = 1.8 \times 10^{-8}$ Ω^{-1} cm^{-1} and $n_c = \sigma/e\mu = 1.3 \times 10^9$ cm^{-3}, respectively. The above results strongly reflect that a greatly reduced trap density and enhanced carrier transport properties of the crystal are achieved by the LCMC method.

These excellent optoelectronic properties mentioned above are also essential for high-performance X-ray detection. Another important parameter for X-ray detection material, the X-ray absorption coefficient, is determined by Z^4/E^3 (where E is the radiation energy), rather than by the optical transition type or bandgap.[5] Firstly, the X-ray absorption coefficient of the $MAPbBr_3$ was determined by using a photon cross-section database.[48] As shown in Fig. 3a, the X-ray absorption coefficient of $MAPbBr_3$ is comparable to that of commercially available detection materials such as CdTe, and much stronger than that of silicon.[48] Fig. 3b shows the attenuation efficiency of these

materials for 50 keV X-rays at different thicknesses. To achieve an attenuation efficiency of 98%, $MAPbBr_3$ only requires a thickness of about 2 mm, while silicon requires a thickness of 73 mm. Therefore, the $MAPbBr_3$ SC is a promising X-ray detection material.

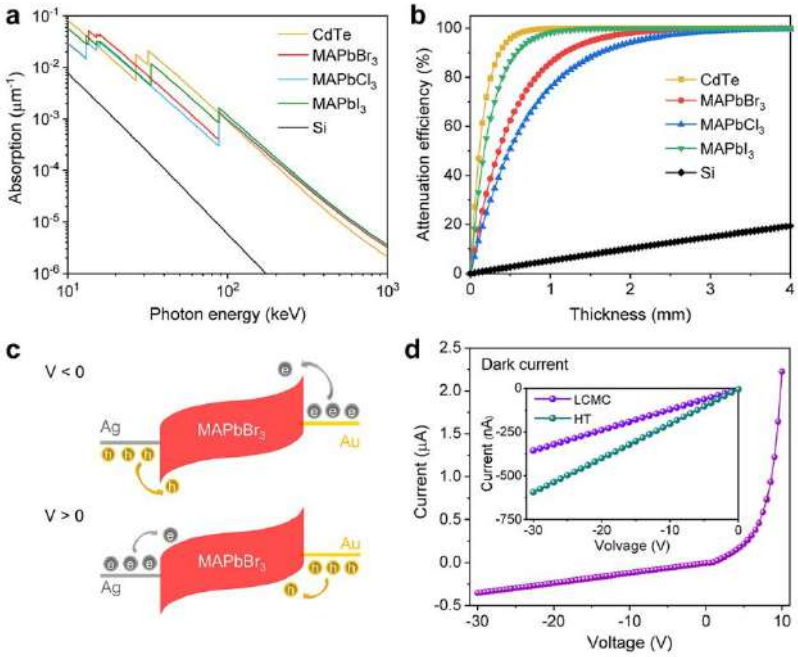

Fig. 3. Architecture and electrical properties of the $MAPbBr_3$ SC X-ray detectors. (a) Absorption coefficients of $MAPbBr_3$, CdTe, $MAPbCl_3$, $MAPbI_3$, and silicon as a function of photon energy. (b) Attenuation efficiency of $MAPbBr_3$, CdTe, $MAPbCl_3$, $MAPbI_3$, and silicon to 50 keV X-ray photons versus thickness. (c) Energy band diagram of the Au/ $MAPbBr_3$ SC/Ag device under reversed bias. (d) Characteristic *I-V* curves of the 2.82 mm-thick LCMC-$MAPbBr_3$ and 2.43 mm-thick HT-$MAPbBr_3$ SC detectors.

The superior properties of the LCMC-$MAPbBr_3$ SCs may exhibit high performance in X-ray detection. Then, X-ray detectors with vertical structure of Au/$MAPbBr_3$ SC/Ag were fabricated, and the effective area of electrodes of all detectors was 0.16 cm^2. As $MAPbBr_3$ is a p-type semiconductor, ohmic and Schottky contacts are formed at the interfaces of Au/$MAPbBr_3$ and Ag/$MAPbBr_3$, respectively. As Au has a higher work function (5.1 eV) than Ag (4.2 eV), the much higher Schottky

barrier potentials are formed at both metal-semiconductor interfaces under reverse bias compared with forward bias (Fig. 3c). Thus, the *I-V* curve exhibit linear and superlinear behavior under reverse and forward bias, respectively. Ga (4.2 eV), which also has a relatively low work function, exhibits similar properties. However, Ga is easily oxidized in the air environment, and its conductivity and other physicochemical properties will be changed, so only Au/$MAPbBr_3$/Ag detectors have been studied. As shown in Fig. 3d, the device exhibits a low dark current at reverse bias and the current increases approximately linearly with increasing voltage, with a dark current of only 0.36 μA at a reverse bias of 30 V. In contrast, it is higher at forward bias and increases exponentially with increasing bias, reaching up to 2.22 μA at 10 V bias. Furthermore, the LCMC-$MAPbBr_3$ SC device exhibits a significantly lower dark current than that of the HT-$MAPbBr_3$ one. Note that the lower the dark current, the higher the weak-signal sensitive performance of the device.[22, 49, 50]

Sensitivity and lowest detectable dose rate are two key figures of merits for X-ray detectors. The sensitivity of a detector can be calculated by the formula $S = I/(D \cdot A)$, where I is the photocurrent ($I = I_{light} - I_{dark}$), D is the dose rate of incident X-ray radiation, A is the effective area of the detector.[49] Fig. 4a shows the photocurrent density as a function of various X-ray dose rates under −20 V bias. The photocurrent density signals generated by both the LCMC-$MAPbBr_3$ and HT-$MAPbBr_3$ SC devices are linearly related to the dose rate. The sensitivity of the 2.82 mm-thick LCMC-$MAPbBr_3$ detector is measured to be 2975.7 μC Gy_{air}^{-1} cm^{-2} at −20 V bias, much higher than that of the 2.43 mm-thick HT-$MAPbBr_3$ one (1068.3 μC Gy_{air}^{-1} cm^{-2}). Furthermore, the lowest detectable X-ray dose rate of the LCMC-$MAPbBr_3$ SC X-ray detector is as low as 0.48 μGy_{air}^{-1} s^{-1}, which is approximately 11 times lower than the 5.5 μGy_{air}^{-1} s^{-1} required for regular medical diagnostics.[51] In addition, the response of the LCMC-$MAPbBr_3$ detector was measured at various bias, as shown in Fig. 4b. Both the photocurrent density and sensitivity of the device improved with the increasing reverse bias voltage, and the photocurrent density generated by the device at the same bias voltage was linearly related to the X-ray dose rate. Fig. 4c shows the sensitivity versus the applied bias voltage, with the sensitivity of the device increasing as the applied bias voltage

increases. Furthermore, the on/off response of the LCMC-$MAPbBr_3$ detector was displayed in Fig. S9 (ESI). The sensitivity of some X-ray detectors based on perovskite materials and the applied bias voltage are shown in Fig. 4d, where the LCMC-$MAPbBr_3$ SC detector exhibits a remarkably high sensitivity.[4, 5, 22, 52–56] After evaluating the X-ray performance by directly comparing LCMC-$MAPbBr_3$ and HT-$MAPbBr_3$ SC devices, the former exhibited significantly higher sensitivity and lower minimum detectable dose rate than the latter. This excellent X-ray detection performance of LCMC-$MAPbBr_3$ based detector may be attributed to the reduced defect density and the improved carrier transport properties.

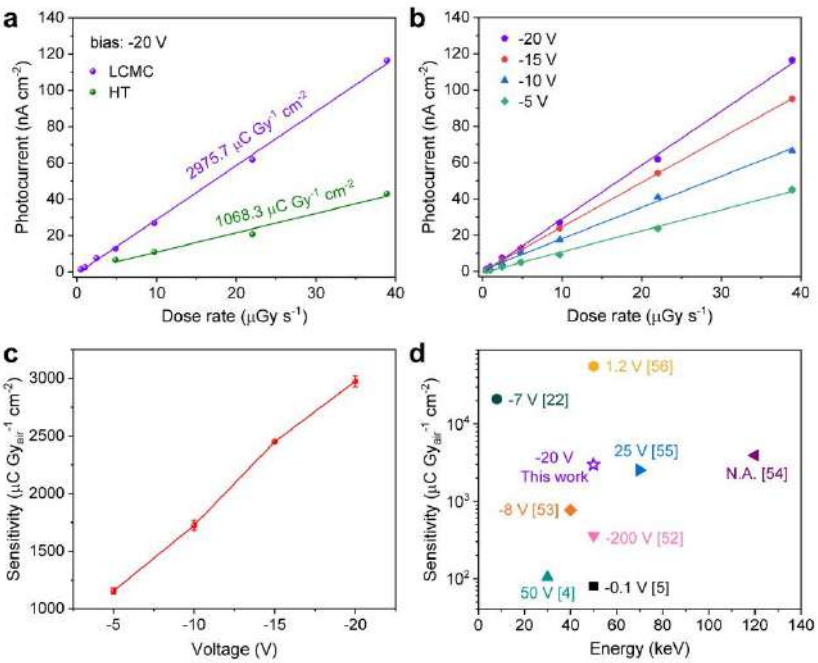

Fig. 4. X-ray detection performance of the $MAPbBr_3$ SC X-ray detectors. (a) X-ray generated photocurrent versus dose rate of 2.82 mm thick LCMC-$MAPbBr_3$ and 2.43 mm thick HT-$MAPbBr_3$ SC detectors under 20 V reverse bias. (b) X-ray generated photocurrent versus dose rate of LCMC-$MAPbBr_3$ SC detectors under different applied biases. (c) Sensitivity under different biases of the LCMC-$MAPbBr_3$ SC detector. (d) Comparison of the sensitivity between the LCMC-$MAPbBr_3$ and perovskite-based X-ray detectors in the literature.

View Article Online
DOI: 10.1039/D2TC00235C

Conclusion

In summary, we have developed a simple, convenient, and highly-reproducible method, LCMC method, to grow high-quality $MAPbBr_3$ SCs at low temperature. By reducing the solubility of $MAPbBr_3$ with formic acid, $MAPbBr_3$ SCs can be prepared at low temperatures and the crystal growth conditions can be maintained in the metastable region by finely controlling the temperature ramp rate, thus suppressing additional crystallization and ensuring high quality crystal growth. The as-obtained $MAPbBr_3$ SCs exhibit extremely low trap density (2.1×10^9 cm^{-3}), high carrier mobility (87.8 cm^2 V^{-1} s^{-1}) and long carrier lifetime (1126 ns), all of which are much better than those prepared by HT method. Moreover, the X-ray detectors based on these LCMC-$MAPbBr_3$ SCs show significantly higher sensitivity of 2975.7 μC Gy_{air}^{-1} cm^{-2} and lower detection limit of 0.48 μGy_{air}^{-1} s^{-1} compared to the HT-$MAPbBr_3$ one.

Supporting Information

Supporting Information is available free of charge on the RSC Publications website.

Acknowledgments

This work is supported by the Young Scientific and Technological Innovation Research Team Funds of Sichuan Province (No. 20CXTD0106), the Fundamental Research Funds for the Central Universities of China (A0920502051619-72) and Foundation of China Academy of Engineering Physics (No. CX2019019, TP02201711).

Author contributions

W.Y., B.G., N.L., and Z.Z. proposed the project. W.Y., B.G., N.L., and W.H. supervised the work. Z.Z., W.L., and W.D. synthesized the sample and fabricated the devices. Z.Z., C.Y., X.P., X.Z., and Y.G. carried out the material characterizations. Z.Z., W.L., W.D., and X.F. carried out the detector measurements and analyzed the results.

Z.Z. analyzed all experimental data. Z.Z., W.Y., B.G., and N.L. wrote the paper with discussion and input from all the authors.

Conflict of interest

The authors declare no conflict of interest.

View Article Online
DOI: 10.1039/D2TC00235C

References

[1] M. Spahn, *Nucl. Instrum. Methods Phys. Res. A*, 2013, **731**, 57–63.

[2] E. Cazalas, B. K. Sarker, M. E. Moore, I. Childres, Y. P. Chen, and I. Jovanovic, *Appl. Phys. Lett.*, 2015, **106**, 223503.

[3] S. Yakunin, M. Sytnyk, D. Kriegner, S. Shrestha, M. Richter, G. J. Matt, H. Azimi, C. J. Brabec, J. Stangl, M. V. Kovalenko and W. Heiss, *Nat. Photon.*, 2015, **9**, 444–449.

[4] W. Pan, H. Wu, J. Luo, Z. Deng, C. Ge, C. Chen, X. Jiang, W.-J. Yin, G. Niu, L. Zhu, L. Yin, Y. Zhou, Q. Xie, X. Ke, M. Sui and J. Tang, *Nat. Photon.*, 2017, **11**, 726–732.

[5] H. Wei, Y. Fang, P. Mulligan, W. Chuirazzi, H.-H. Fang, C. Wang, B. R. Ecker, Y. Gao, M. A. Loi, L. Cao and J. Huang, *Nat. Photon.*, 2016, **10**, 333–339.

[6] S O. Kasap, *J. Phys. D*, 2000, **33**, 2853.

[7] D. J. Brenner, C. D. Elliston, E. J. Hall and W. E. Berdon, *Am. J. Roentgenol.*, 2001, **176**, 289–296.

[8] Z. Zhu, W. Deng, W. Li, F. Chun, C. Luo, M. Xie, B. Pu, N. Lin, B. Gao and W. Yang, *Adv. Mater. Interfaces*, 2021, **8**, 2001812.

[9] W. Li, D. Xiong, M. Xie, C. Luo, X. Zeng, Y. Gao, B. Guo, C. Yan, F. Chun, Z. Zhu, X. Fan, W. Deng and W. Yang, *J. Mater. Chem. C*, 2020, **8**, 3491.

[10] Y. Yang, Y. Yan, M. Yang, S. Choi, K. Zhu, J. M. Luther and M. C. Beard, *Nat. Commun.*, 2015, **6**, 7961.

[11] Y. Huang, Y. Zhang, J. Sun, X. Wang, J. Sun, Q. Chen, C. Pan and H. Zhou, *Adv. Mater. Interfaces*, 2018, **5**, 1800224.

[12] Y. Zhang, Y. Liu, Z. Yang, M. Chen and S. Liu, *Adv. Func. Mater.*, 2020, **30**, 2002742.

[13] B. Murali, H. K. Kolli, J. Yin, R. Ketavath, O. M. Bakr and O. F. Mohammed, *ACS Mater. Lett.*, 2020, **2**, 184.

[14] J. Li, Z. Han, Y. Gu, D. Yu, J. Liu, D. Hu, X. Xu and H. Zeng, *Adv. Func. Mater.*, 2021, **31**, 2008684.

View Article Online
DOI: 10.1039/D2TC00235C

[15] T. Zuo, X. He, P. Hu and H. Jiang. *ChemNanoMat*, 2019, **5**, 278.

[16] M. I. Saidaminov, A. L. Abdelhady, B. Murali, E. Alarousu, V. M. Burlakov, W. Peng, I. Dursun, L. Wang, Y. He, G. Maculan, A. Goriely, T. Wu, O. F. Mohammed and O. M. Bakr, *Nat. Commun.*, 2015, **6**, 7586.

[17] G. E. Eperon, S. D. Stranks, C. Menelaou, M. B. Johnston, L. M. Herza and H. J. Snaith, *Energy Environ. Sci.*, 2014, **7**, 982–988.

[18] Y. Bi, E. M. Hutter, Y. Fang, Q. Dong, J. Huang and T. J. Savenije, *J. Phys. Chem. Lett.*, 2016, **7**, 923–928.

[19] Z. Lian, Q. Yan, T. Gao, J. Ding, Q. Lv, C. Ning, Q. Li and J.-l. Sun, *J. Am. Chem. Soc.*, 2016, **138**, 9409–9412.

[20] M. I. Saidaminov, V. Adinolfi, R. Comin, A. L. Abdelhady, W. Peng, I. Dursun, M. Yuan, S. Hoogland, E. H. Sargent and O. M. Bakr, *Nat. Commun.*, 2015, **6**, 8724.

[21] L. Lee, J. Baek, K. S. Park, Y.-E. Lee, N. K. Shrestha and M. M. Sung, *Nat. Commun.*, 2017, **8**, 15882.

[22] W. Wei, Y. Zhang, Q. Xu, H. Wei, Y. Fang, Q. Wang, Y. Deng, T. Li, A. Gruverman, L. Cao and J. Huang, *Nat. Photon.*, 2017, **11**, 315–321.

[23] H.-S. Rao, B.-X. Chen, X.-D. Wang, D.-B. Kuang and C.-Y. Su, *Chem. Commun.*, 2017, **53**, 5163–5166.

[24] Y. Zhou, C. Li, Y. Wang, X. Du, P. Liu and W. Xie, *IOP Conf. Ser.: Mater. Sci. Eng.*, 2017, **167**, 012019.

[25] C. Liu, Y.-B. Cheng and Z. Ge, *Chem. Soc. Rev.*, 2020, **49**, 1653–1687.

[26] P. K. Nayak, D. T. Moore, B. Wenger, S. Nayak, A. A. Haghighirad, A. Fineberg, N. K. Noel, O. G. Reid, G. Rumbles, P. Kukura, K. A. Vincent and H. J. Snaith, *Nat. Commun.*, 2016, **7**, 13303.

[27] Y. Liu, Y. Zhang, Z. Yang, J. Feng, Z. Xu, Q. Li, M. Hu, H. Ye, X. Zhang, M. Liu, K. Zhao and S. Liu, *Mater. Today*, 2019, **22**, 67–75.

[28] F. Yao, J. Peng, R. Li, W. Li, P. Gui, B. Li, C. Liu, C. Tao, Q. Lin and G. Fang, *Nat. Commun.*, 2020, **11**, 1194.

[29] J. Frenkel, *J. Chem. Phys.*, 1939, **7**, 538.

View Article Online
DOI: 10.1039/D2TC00235C

[30] J. B. Zeldovich, *J. Exp. Theor. Phys.*, 1942, **12**, 525.

[31] R. Strey, P. E. Wagner and Y. Viisanen, *J. Phys.Chem.*, 1994, **98**, 7748–7758.

[32] J. W. Mullin, Crystallization, 4th ed., Butterworth-Heinemann: Oxford, 2001**.**

[33] M. I. Saidaminov, A. L. Abdelhady, G. Maculan and O. M. Bakr, *Chem. Commun.*, 2015, **51**, 17658–17661.

[34] Y. Liu, Z. Yang, D. Cui, X. Ren, J. Sun, X. Liu, J. Zhang, Q. Wei, H. Fan, F. Yu, X. Zhang, C. Zhao and S. Liu, *Adv. Mater.*, 2015, **27**, 5176–5183.

[35] J. Ding, Y. Zhao, S. Du, Y. Sun, H. Cui, X. Zhan, X. Cheng and L. Jing, *J. Mater. Sci.*, 2017, **52**, 7907–7916.

[36] M.-H. Sung, J.-S. Kim, W.-S. Kim, I. Hirasawa and W.-S. Kim, *J. Cryst. Growth*, 2002, **235**, 529–540.

[37] W. Peng, L. Wang, B. Murali, K.-T. Ho, A. Bera, N. Cho, C.-F. Kang, V. M. Burlakov, J. Pan, L. Sinatra, C. Ma, W. Xu, D. Shi, E. Alarousu, A. Goriely, J.-H. He, O. F. Mohammed, T. Wu and O. M. Bakr, *Adv. Mater.*, 2016, **28**, 3383–3390.

[38] A. A. Zhumekenov, V. M. Burlakov, M. I. Saidaminov, A. Alofi, M. A. Haque, B. Turedi, B. Davaasuren, I. Dursun, N. Cho, A. M. El-Zohry, M. D. Bastiani, A. Giugni, B. Torre, E. D. Fabrizio, O. F. Mohammed, A. Rothenberger, T. Wu, A. Goriely and O. M. Bakr, *ACS Energy Lett.*, 2017, **2**, 1782–1788.

[39] D. Shi, V. Adinolfi, R. Comin, M. Yuan, E. Alarousu, A. Buin, Y. Chen, S. Hoogland, A. Rothenberger, K. Katsiev, Y. Losovyj, X. Zhang, P. A. Dowben, O. F. Mohammed, E. H. Sargent and O. M. Bakr, *Science*, 2015, **347**, 519-522.

[40] B. Murali, E. Yengel, C. Yang, W. Peng, E. Alarousu, O. M. Bakr and O. F. Mohammed, *ACS Energy Lett.*, 2017, **2**, 846–856.

[41] Y. Liu, Y. Zhang, K. Zhao, Z. Yang, J. Feng, X. Zhang, K. Wang, L. Meng, H. Ye, M. Liu and S. Liu, *Adv. Mater.*, 2018, **30**, 1707314.

[42] P. Mark and W. Helfrich, *J. Appl. Phys.*, 1962, **33**, 205.

[43] R. H. Bube, *J. Appl. Phys.*, 1962, **33**, 1733.

[44] A. Poglitsch and D. Weber, *J. Chem. Phys.*, 1987, **87**, 6373.

[45] J. Feng, X. Yan, Y. Liu, H. Gao, Y. Wu, B. Su and L. Jiang, *Adv. Mater.*, 2017, **29**, 1605993.

[46] G. Maculan, A. D. Sheikh, A. L. Abdelhady, M. I. Saidaminov, M. A. Haque, B. Murali, E. Alarousu, O. F. Mohammed, T. Wu and O. M. Bakr, *J. Phys. Chem. Lett.*, 2015, **6**, 3781–3786.

[47] Q. Dong, Y. Fang, Y. Shao, P. Mulligan, J. Qiu, L. Cao and J. Huang, *Science*, 2015, **347**, 967–970.

[48] M. J. Berger, J. H. Hubbell, S. M. Seltzer, J. Chang, J. S. Coursey, R. Sukumar, D. S. Zucker and K. Olsen, XCOM: Photon Cross Sections Database. http://physics.nist.gov/xcom (accessed: June, 2021).

[49] V. F. Dvoryankin, G. G. Dvoryankina, A. A. Kudryashov, A. G. Petrov, V. D. Golyshev and S. V. Bykova, *Tech. Phys.*, 2010, **55**, 306–308.

[50] H. Wei, D. DeSantis, W. Wei, Y. Deng, D. Guo, J. S. Tom, L. Cao and J. Huang, *Nat. Mater.*, 2017, **16**, 826–833.

[51] I. Clairand, J.-M. Bordy, E. Carinou, J. Daures, J. Debroas, M. Denozière, L. Donadille, M. Ginjaume, C. Itié, C. Koukorava, S. Krim, A.-L. Lebacq, P. Martin, L. Struelens, M. Sans-Merce and F. Vanhavere, *Radiat. Meas.*, 2011, **46**, 1252–1257.

[52] Q. Xu, W. Shao, Y. Li, X. Zhang, X. Ouyang, J. Liu, B. Liu, Z. Wu, X. Ouyang, X. Tang and W. Jia, *ACS Appl. Mater. Interfaces*, 2019, **11**, 9679–9684.

[53] Q. Xu, X. Wang, H. Zhang, W. Shao, J. Nie, Y. Guo, J. Wang and X. Ouyang, *ACS Appl. Electron. Mater.*, 2020, **2**, 879–884.

[54] J. Song, X. Feng, H. Li, W. Li, T. Lu, C. Guo, H. Zhang, H. Wei and B. Yang, *J. Phys. Chem. Lett.*, 2020, **11**, 3529–3535.

[55] S. Shrestha, R. Fischer, G. J. Matt, P. Feldner, T. Michel, A. Osvet, I. Levchuk, B. Merle, S. Golkar, H. Chen, S. F. Tedde, O. Schmidt, R. Hock, M. Rührig, M. Göken, W. Heiss, G. Anton and C. J. Brabec, *Nat. Photon.*, 2017, **11**, 436–440.

[56] W. Pan, B. Yang, G. Niu, K.-H. Xue, X. Du, L. Yin, M. Zhang, H. Wu, X.-S. Miao and J. Tang, *Adv. Mater.*, 2019, **31**, 1904405.